



## Strong ground motion estimation in the Sea of Marmara region (Turkey) based on a scenario earthquake

Nelson Pulido<sup>a,\*</sup>, Anibal Ojeda<sup>b</sup>, Kuvvet Atakan<sup>b</sup>, Tetsuo Kubo<sup>c</sup>

<sup>a</sup>*Earthquake Disaster Mitigation Research Center EDM, NIED, 4F Human Renovation Museum, 1-5-2, Kaigan-dori, Wakahama, Chuo-ku, Kobe 651-0073, Japan*

<sup>b</sup>*Department of Earth Science, University of Bergen, Allégt. 41, N-5007, Bergen, Norway*

<sup>c</sup>*Earthquake Disaster Mitigation Research Center EDM, NIED/School of Engineering, The University of Tokyo, Bunkyo-ku, Tokyo 113-8656, Japan*

Accepted 3 June 2004

### Abstract

We perform a broadband frequency bedrock strong ground motion simulation in the Marmara Sea region (Turkey), based on several fault rupture scenarios and a source asperity model. The technique combines a deterministic simulation of seismic wave propagation at low frequencies with a semi-stochastic procedure for the high frequencies. To model the high frequencies, we applied a frequency-dependent radiation pattern model, which efficiently removes the effective dependence of the pattern coefficient on the azimuth and take-off angle as the frequency increases. The earthquake scenarios considered consist of the rupture of the closest segments of the North Anatolian Fault System to the city of Istanbul. Our scenario earthquakes involve the rupture of the entire North Anatolian Fault beneath the Sea of Marmara, namely the combined rupture of the Central Marmara Fault and North Boundary Fault segments. We defined three fault rupture scenarios based on the location of the hypocenter, selecting a preferred hypocentral location near a fault bend for each case. We analysed the effect of location of the asperity, within the Central Marmara Fault, on the subsequent ground motion, as well as the influence of anelasticity on the high-frequency attenuation characteristics. The fault and asperity parameters for each scenario were determined from empirical scalings and from results of kinematic and dynamic models of fault rupture. We calculated the resulting time series and spectra for ground motion at Istanbul and evaluated the sensitivity of the predictions to choice of model parameters. The location of the hypocenter is thus shown to be a critical parameter for determining the worst scenario earthquake at Istanbul. We also found that anelasticity has a significant effect on the regional attenuation of peak ground accelerations. Our simulated ground motions result in large values of acceleration response spectra at long periods, which could be critical for building damage at Istanbul during an actual earthquake.

© 2004 Elsevier B.V. All rights reserved.

*Keywords:* Strong motion simulation; Earthquake scenario; Seismic hazard; North Anatolian fault

\* Corresponding author. Tel.: +81 78 262 5530; fax: +81 78 262 5527.

*E-mail address:* [nelson@edm.bosai.go.jp](mailto:nelson@edm.bosai.go.jp) (N. Pulido).

## 1. Introduction

Following the disastrous Izmit and Duzce earthquakes on the North Anatolian Fault (NAF) in 1999, the earthquake hazard in Istanbul has become a great concern. In this study, we perform a strong ground motion simulation for the Sea of Marmara region with emphasis in Istanbul, based on a fault rupture scenario in the Sea of Marmara. In recent years, extensive multi-channel seismic reflection surveys in the Sea of Marmara have become available, allowing investiga-

tion of the complex geometry of the western North Anatolian fault (e.g., Okay et al., 2000; Aksu et al., 2000; Imren et al., 2001). The NAF locally consists of three fault segments with subsidiary branches. For this simulation, we used the model for the Marmara region by Okay et al. (2000). For our earthquake scenario, we selected the Central Marmara Fault (CMF) and North Boundary Fault (NBF) segments, which are the closest to Istanbul and thus pose the largest hazard to this city (Fig. 1). Although there is detailed information about the geometry of these fault segments geometry at

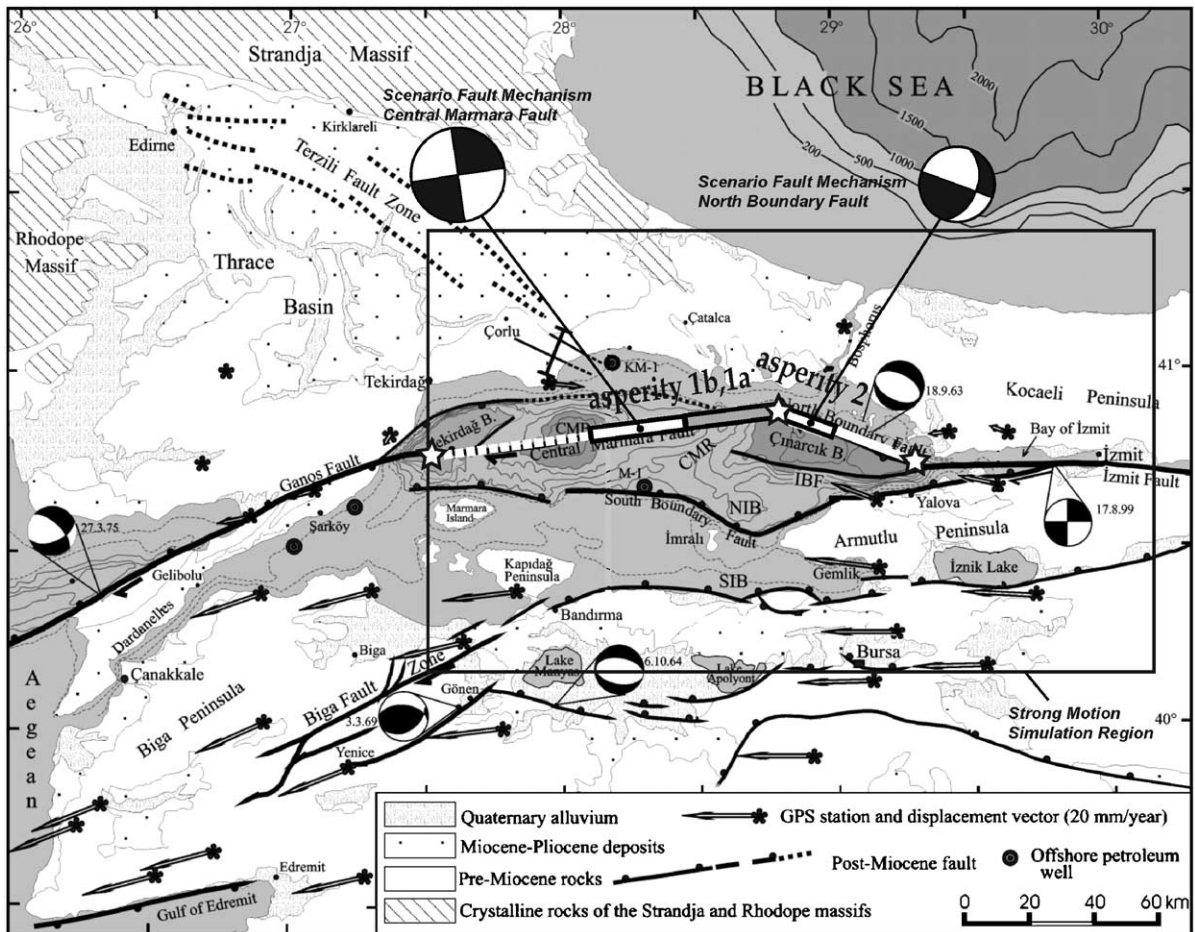


Fig. 1. Map of active faulting in the Sea of Marmara region (after Okay et al., 2000). The assumed fault ruptures of the scenario earthquakes are shown by a dashed white line (Central Marmara Fault) and a continuous white line (North Boundary Fault). The epicenter of the three scenario earthquakes is shown by a star. Scenario 1a and 1b differs only by the location of the asperity within the CMF segment (asperities 1a and 1b, in a light gray and white line, respectively). Asperity 2 within the NBF segment is also shown by a white line. The assumed focal mechanism for each fault segment is shown (as lower focal hemisphere, equal area projections). The box shows the target region for the strong motion simulation. CMB is the Central Marmara Basin. CMB is the Central Marmara basin; SIB is the South İmralı Basin; NIB is the North İmralı Basin; CMR is the Central Marmara Ridge; IBF is the Inner Boundary Fault.

shallow (up to ~5 km) depths, there is major uncertainty concerning their deeper parts. We thus assumed that at depth these fault segments dip vertically. Concerning the fault mechanisms, GPS results show a regional displacement vector almost parallel to CMF (Straub et al., 1997), which supports the idea of purely right-lateral strike-slip for that segment. However, the NBF is highly oblique to the regional displacement, suggesting the possibility of an oblique normal mechanism. We assumed a seismogenic zone 20 km deep based on observed depth distributions of seismicity (Gurbuz et al., 2000). Recent seismic observations within the Sea of Marmara using Ocean Bottom Seismographs, have revealed significant microseismic activity on the CMF and NBF (Sato et al., 2004), which suggests that much of the slip in the region is likely to be accommodated seismically. All our scenario earthquakes involve the combined rupture of the CMF and NBF segments. This is because it has been observed that the NAF is continuous beneath the Sea of Marmara (Okay et al., 2000; Le Pichon et al., 2001), so it has no significant fault offsets that could stop a fault rupture. It could be argued that the significant bend between the CMF and NBF (~30°) could be enough to stop a fault rupture. However, recent dynamic models of faulting have shown that even large fault bends cannot arrest a fault rupture (Poliakov et al., 2002; Kame et al., 2003). The recent Izmit earthquake indeed provided a good example of a fault rupture running across a significant fault bend (Harris et al., 2002). Although fault bends do not stop fault ruptures, observations of past crustal earthquakes have shown that they are preferred sites for the initiation of rupture (e.g., King and Nabelek, 1985). We therefore decided to locate the hypocenter of each of our scenario earthquakes near a fault bend. We assumed three fault rupture scenarios based on the location of the hypocenter (Fig. 2). The fault rupture parameters were determined by assuming a dynamic asperity model (Das and Kostrov, 1986) and by empirical scaling of asperity area to fault rupture area (Somerville et al., 1999).

Recently, hybrid techniques have been successfully applied for the simulation of the near-fault ground motion in intermediate to large crustal earthquakes (e.g., Kamae et al., 1998; Pitarka et al., 2000; Pulido and Kubo, 2004). Although low-frequency ground motion is now well understood, knowledge of high frequency ground motion is still limited. To improve

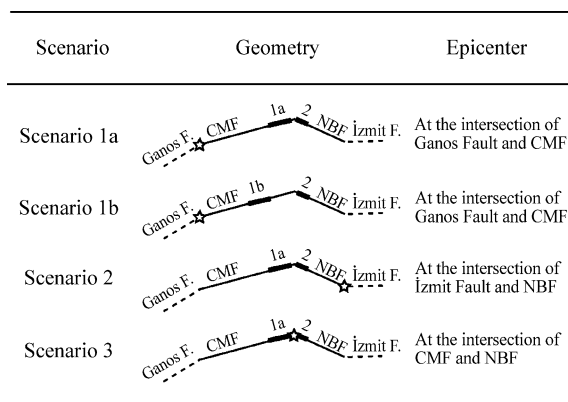


Fig. 2. Geometry of the models used to define the scenario earthquakes. Note that asperities 1a and 1b have the same parameters but different locations.

the accuracy of simulations of high frequency ground motion, it is necessary to better understand the characteristics of high-frequency radiation near seismic sources. Analyses of strong-motion records of recent earthquakes suggest that the radiation pattern, as observed at the surface, has a strong dependence on frequency (Akazawa and Kagawa, 2000; Satoh, 2002a,b; Takenaka et al., 2003). In the present study, we apply a ground motion simulation technique that uses a frequency-dependent radiation-pattern model to simulate high-frequency ground motion (Pulido and Kubo, 2004). This model efficiently removes the frequency-dependence of the radiation pattern coefficient on the azimuth and take-off angle of raypaths at asperities.

## 2. Methodology for ground motion estimation

We estimated the near fault ground motion using a broadband (0.1 to 10 Hz) hybrid simulation technique, which combines deterministic modelling of wave propagation at low frequencies with a semi-stochastic technique for the high frequencies. The idea is to evaluate the strong ground motion radiated from a finite fault, multi-asperity source model. The total ground motion radiated at each asperity is obtained by adding the low-frequency and high-frequency waveforms in time domain. Details of the simulation technique are explained in Pulido and Kubo (2004). The methodology is briefly outlined as follows.

### 2.1. Low-frequency ground motion

For the low-frequency (0.1 to 1 Hz) ground motion, asperities are subdivided into several point sources, and the time delayed ground motions from them is added, assuming a constant rupture velocity. The seismogram from each point source is obtained numerically by the discrete wave number method of Bouchon (1981), which computes wave propagation in a flat-layered velocity structure, for a particular focal mechanism and source time function.

### 2.2. High-frequency ground motion

The high-frequency (1 to 10 Hz) ground motion is calculated for a finite asperity consisting of several subfaults as before. The ground motion from each subfault is obtained using a technique based on the stochastic approach of Boore (1983), summation being performed by the empirical Green's function method (Irikura, 1986), which is very efficient for radiation at high frequencies from finite faults. Boore's (1983) procedure was modified by Pulido and Kubo (2004), by introducing a frequency-dependent radiation pattern ( $R_p$ ) into the ground motion acceleration spectrum (see below). The radiation pattern coefficient  $R_{pi}$  at a particular receiver for the  $i$ 'th component of ground motion is obtained as follows:

$$\begin{aligned}
 R_{pi}(\theta, \phi, f) &= F_i(\phi_s, \delta, \lambda, \theta, \phi) \quad \text{for } f \leq f_1 \\
 R_{pi}(\theta, \phi, f) &= F_i(\phi_s, \delta, \lambda, \theta, \phi) \\
 &\quad + \left[ R_{S,ave} / \sqrt{2} - F_i(\phi_s, \delta, \lambda, \theta, \phi) \right] \\
 &\quad \times (f - f_1) / (f_2 - f_1) \quad \text{for } f_1 < f < f_2 \\
 R_{pi}(\theta, \phi, f) &= R_{S,ave} / \sqrt{2} \quad \text{for } f \geq f_2
 \end{aligned} \tag{1}$$

where  $F_i(\phi_s, \delta, \lambda, \theta, \phi)$  is the  $i$ 'th component ( $ns$ ,  $ew$  or  $ud$ ) of the theoretical radiation pattern coefficient of a double-couple with strike  $\phi_s$ , dip  $\delta$  and rake  $\lambda$ , at a receiver with take-off angle  $\theta$  and azimuth  $\phi$  (Aki and Richards, 2002, Eqs. 4.88, 4.90 and 4.91). Only contributions from the SH and SV radiation pattern coefficients are considered. The idea behind Eq. (1) is to apply a smooth transition

from  $F_i$  to an average radiation pattern coefficient ( $R_{S,ave}$ ) as the frequency increase. We assume a linear variation of  $R_{pi}$  from a frequency  $f_1$  to a frequency  $f_2$ , with  $f_1=1$  Hz and  $f_2=3$  Hz.

$R_{S,ave}$  is the average radiation pattern coefficient for the total S-wave, calculated for all rays departing in the upper focal hemisphere ( $\theta$  from  $90^\circ$  to  $180^\circ$ ) which corresponds to paths to stations in the near-fault region, and divided by  $\sqrt{2}$  to account for the partitioning of the S-wave into two components.  $R_{S,ave}$  is calculated as

$$R_{S,ave} = \left( \sum_{i=SH,SV} \left( \frac{\iint F_i(\phi_s, \delta, \lambda, \theta, \phi) \sin \theta \, d\phi d\theta}{\iint \sin \theta \, d\phi d\theta} \right)^2 \right)^{1/2} \tag{2}$$

Boore and Boatwright (1984). Using Eq. (2) we obtained a  $R_{S,ave}$  value of 0.55 for a vertical strike-slip fault.

According to the formal definition of the radiation pattern from a source (Aki and Richards, 2002, Eqs. 4.89, 4.90 and 4.91), radiation pattern coefficients are frequency-independent. However, Takenaka et al. (2003) have observed that aftershocks of the March 26 and May 13, 1997 Northwestern Kagoshima (Japan) earthquakes did not show a radiation pattern predicted from a double-couple source for high frequencies, even though the low frequency components showed the standard double-couple radiation. To arrive to this conclusion, Takenaka et al. (2003) examined the ratio between tangential and radial components of ground motion for different frequency bands. These analyses led Takenaka et al. (2003) to conclude that the radiation patterns of SH and SV waves are purely stochastic at high frequencies. Takenaka et al. (2003) ascribed this stochastic nature to strong SH and SV mixing or coupling induced by local structural effects. Akazawa and Kagawa (2000) and Satoh (2002a) reached similar conclusions. We thus decided to incorporate a frequency dependence on the radiation pattern coefficient to take into account the effect of scattering from a heterogenous structure in the near-fault region, at high frequencies, and this led to the use of an averaged radiation pattern coefficient for high-frequency seismic radiation in all directions, as specified above.

### 3. Scenario earthquakes in the sea of Marmara region

Selection of the starting point of fault rupture is a very important issue, since it will determine the regions that will experience ground motion amplified by forward directivity. Observations from several large crustal earthquakes suggest that rupture initiation is confined to sites near fault bends (e.g., King and Nabelek, 1985), a view confirmed by dynamic rupture models of faults with large bends (Andrews, 1989). We thus located the initiation of rupture at a fault bend for each scenario earthquake: at the intersection of the CMF and Ganos Fault in scenarios 1a and 1b; at the intersection of the Izmit Fault and the NBF in scenario 2; and at the intersection of the CMF and NBF in scenario 3 (Fig. 2). We located the hypocenter at a depth of 10 km for all our scenarios. In order to study the influence of the location of other asperities within fault segments, we consider two different locations of the asperity within the CMF. Scenario 1a is defined with an asperity located near the fault bend between the CMF and NBF (asperity 1a), and scenario 1b has an asperity located at the central part of the CMF (asperity 1b) (Figs. 1 and 2). Except for the locations of asperities, scenarios 1a and 1b are identical.

The most important parameter for characterizing each earthquake scenario is the total seismic moment. We decided to use a value of  $2.0 \times 10^{20}$  Nm, obtained by averaging results from USGS moment tensor solutions (cf. Sipkin, 1982), the Harvard CMT catalogue (cf. Dziewonski et al., 1981), and from Yagi and Kikuchi (2000), Bouchon et al. (2002), Sekiguchi and Iwata (2002), Xu et al. (2002) and Delouis et al. (2002) for the

1999 Izmit earthquake, which had the same rupture length as each of our scenario earthquakes.

### 4. Estimation of source parameters

#### 4.1. Properties of asperities

The most important asperity parameters are its area, location, stress drop, seismic moment, rise time and rupture velocity. The total asperity area  $S_a$  for every fault segment of fault rupture area  $S$  was calculated using the empirical ratio (Somerville et al., 1999):

$$S_a/S = 0.22 \quad (3)$$

The locations of the asperities in each fault plane were defined by considering the seismicity. The hypocenter distribution in the west of the Sea of Marmara, associated with the CMF, decreases abruptly to the east of this segment, near the eastern margin of the Central Marmara Basin (CMB in Fig. 1), suggesting a seismic gap (Gurbuz et al., 2000). However, it has been observed (Wiemer and Wyss, 1997) that highly stressed asperities may be defined by anomalously low  $b$  values (i.e., by low microseismicity). Considering the previous observations, we decided to locate all our asperities within this seismic gap region. The location of asperities and fault geometry of scenario 1a is shown in Figs. 2 and 3. Scenario 1b differs from scenario 1a only with regard to the location of the asperity within the CMF (dotted box in Fig. 3). Scenarios 2 and 3 have identical fault and asperity configuration to scenario 1a, but different hypocenter location (Fig. 2). The location

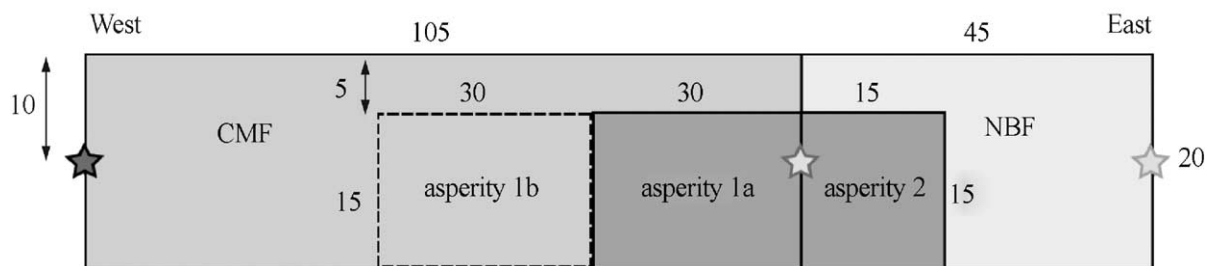


Fig. 3. Fault and asperity geometry for scenario 1a. Asperities for this scenario are depicted by dark gray boxes (asperity 1a and asperity 2). The dotted box corresponds to the location of the asperity 1b within the CMF (scenario 1b). A dark gray star depicts the hypocenter location of scenarios 1a and 1b. The light gray stars correspond to the hypocenter location of scenarios 2 and 3.

Table 1  
Fault segment parameters

Fault Segment/Asperity	Area (km <sup>2</sup> )	Mechanism			Western edge		Eastern edge	
		strike	dip	rake	longitude (°E)	latitude (°N)	longitude (°E)	latitude (°N)
CMB	105×20	81.5	90	180	27.570	40.735	28.800	40.870
NBF	45×20	110	90	−135	28.800	40.870	29.305	40.732
Asperity 1a	30×15	81.5	90	180	28.477	40.835	28.800	40.870
Asperity 1b	30×15	81.5	90	180	28.160	40.800	28.477	40.835
Asperity 2	15×15	110	90	−135	28.800	40.870	28.970	40.825

Areas of rectangular model fault planes are specified as their length×their width. Length, strike and dip of model fault planes are based on Okay et al. (2000). Widths of model fault planes are based on Gurbuz et al. (2000).

and parameters of fault segments and asperities are listed in Tables 1 and 2.

#### 4.2. Stress drop and seismic moment

Results from a dynamic model for rupture of a circular fault (with radius  $R$ ) with an asperity (with radius  $r$ ) at its center (Das and Kostrov, 1986) suggest that the ratio between the asperity stress drop and the fault average stress drop is approximately equal to  $r/R$ . This combined with Eq. (3) yields a value for this ratio of 0.47. The total seismic moment for an asperity model can be calculated as:

$$M_o = (16/7)\Delta\sigma_{ave}rR^2(24/7\pi)^2 \quad (4)$$

(Das and Kostrov, 1986). Substituting Eq. (3) into Eq. (4), we obtain:

$$M_o = 0.229\Delta\sigma_{ave}S^{3/2} \quad (5)$$

Eq. (5) gives the total seismic moment of the asperity model (in Nm) in terms of the average stress drop  $\Delta\sigma_{ave}$ , and the total rupture area  $S$  (m<sup>2</sup>). For the seismic moment of  $2.0 \times 10^{20}$  Nm, we obtain an average stress drop of  $\sim 5.0$  MPa from Eq. (5). We assumed that the latter value of stress drop is equal to the background region stress drop of our scenario earthquakes. This assumption is justified because the asperity area is specified as only 20% of the total area so a weighted average of the stress drop across the fault plane will be close to the background stress drop value. The asperity stress drop is about twice the average stress drop, namely 10 MPa in our case. Finally, we can calculate the asperity seismic moment ( $M_{asp}$ ) using the Brune relationship between stress

drop, seismic moment and asperity area (Brune, 1970) as follows:

$$M_{asp} = (16/7)\Delta\sigma_a(S_a/\pi)^{3/2} \quad (6)$$

where  $S_a$  and  $\Delta\sigma_a$  are the asperity area and stress drop.

#### 4.3. Rise time

We selected a rise time of 3 s for all our scenario earthquakes, consistent with a kinematic source model of the 1999 Izmit earthquake (Bouchon, 1981).

#### 4.4. Rupture velocity

Rupture velocity is controlled by a delicate balance between the consumed fracture energy of the fault and

Table 2  
Asperity model parameters

Parameter	Value	
	Asperity 1a, 1b	Asperity 2
Stress drop (bar)	100	100
Seismic Moment ( $10^{18}$ Nm)	41.5	14.7
Rise time (s)	3.0	3.0
Rupture velocity (km/s)	2.8 to 3.2	2.8 to 3.2
Number of model subfaults	50	25
Q (for moderate attenuation)	$50 f^{1.09}$	$50 f^{1.09}$
Q (for low attenuation)	$100 f^{1.5}$	$100 f^{1.5}$
$f_{max}$ (Hz)	10	10

Asperities 1a and 1b are defined with identical parameters but at different locations. Stress drop is expressed as  $2 \times \Delta\sigma_{ave}$  where  $\Delta\sigma_{ave}$  is the fault average stress drop. The frequency-dependence of the anelasticity quality factor Q for moderate attenuation is from Gurbuz et al. (2000). The alternative for low attenuation is suggested in this study.

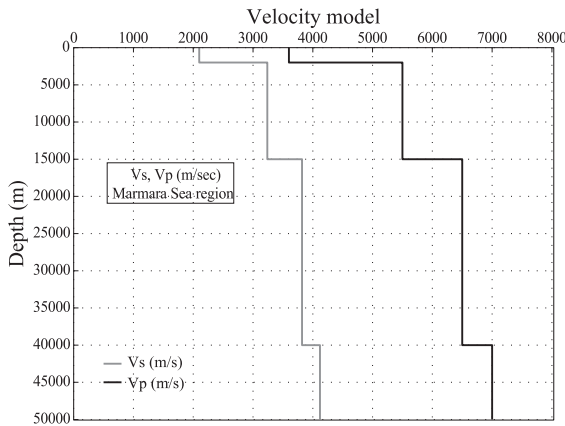


Fig. 4. Crustal velocity model of the Marmara Sea region (Şarif Barış, personal communication, 2003).

the supplied elastic strain energy (Fukuyama and Madariaga, 2000). Since our model is kinematic, we have to fix a priori the rupture velocity. We used an average value of 3.0 km/s, from a kinematic model of the 1999 Izmit earthquake (Bouchon, 1981). According to that model most of the rupture propagated at a sub-Rayleigh speed of ~3.0 km/s. To enhance the high-frequency radiation from our model, we allowed the rupture velocity to vary randomly from 2.8 to 3.2. This corresponds to a range from a sub-Rayleigh to a Rayleigh (0.9  $V_s$ ) rupture velocity.

#### 4.5. Background moment

In addition to the asperity seismic moment, we assumed a background slip at every fault segment in order to match the total seismic moment of the fault. The background seismic moment was calculated proportionally to the asperity seismic moment for each fault segment.

#### 4.6. Velocity structure

For simulation of the low-frequency wave propagation, we used a one-dimensional crustal velocity model, as is used for routine earthquake location in the Sea of Marmara region (Fig. 4). We simulated broadband ground motion across a region of 200×120 km (Fig. 1) with a grid spacing of 10 km. We also calculated the ground motion time series and spectra at three target sites in the Istanbul city (Table 3). HIS is in the historical center of Istanbul (Sultanahmet district). BUS is in the central business district (Şişli). SIT is located west of Istanbul in the Avcılar district, which was heavily damaged during the 1999 Kocaeli (Turkey) earthquake due to local site effects (e.g., Özel et al., 2002, 2004; Ergin et al., 2004).

#### 4.7. $Q$ and $f_{max}$

The high frequency content of simulated ground motions is mainly controlled by anelastic attenuation of S-waves, and the cut-off frequency  $f_{max}$  beyond which the acceleration spectrum decays sharply with increasing frequency (e.g., Pulido and Kubo, 2004). To study the effect of  $Q$  on the simulated ground motion we considered two cases: (1) a moderate value of  $Q$  found from a seismic experiment in the Marmara region (Gündüz et al., 1998), hereafter referred to as the “Moderate Attenuation Model”:

$$Q = 50 f^{1.09} \tag{7}$$

and (2) the “Low Attenuation Model”, an arbitrary choice designed to produce higher  $Q$  at each

Table 3  
Model station parameters

Station	Longitude (°E)	Latitude (°N)	Scenario 1a [1]		Scenario 1a [2]		Scenario 1b		Scenario 2		Scenario 3	
			PGA (cm/s <sup>2</sup> )	PGV (cm/s)	PGA (cm/s <sup>2</sup> )	PGV (cm/s)	PGA (cm/s <sup>2</sup> )	PGV (cm/s)	PGA (cm/s <sup>2</sup> )	PGV (cm/s)	PGA (cm/s <sup>2</sup> )	PGV (cm/s)
SIT	28.680	40.990	228	63	334	71	321	64	194	31	211	23
HIS	28.950	41.010	141	64	234	64	259	67	180	27	128	16
BUS	29.040	41.090	108	47	146	47	134	53	115	13	91	16

As explained in the text, SIT, HIS and BUS are three sets of notional station coordinates in different parts of Istanbul. PGA and PGV are peak ground acceleration and velocity. For scenario 1a, solution [1] is for the “Moderate Attenuation Model” whereas solution [2] and the solutions for all other scenarios are for the “Low Attenuation Model” (Table 2).

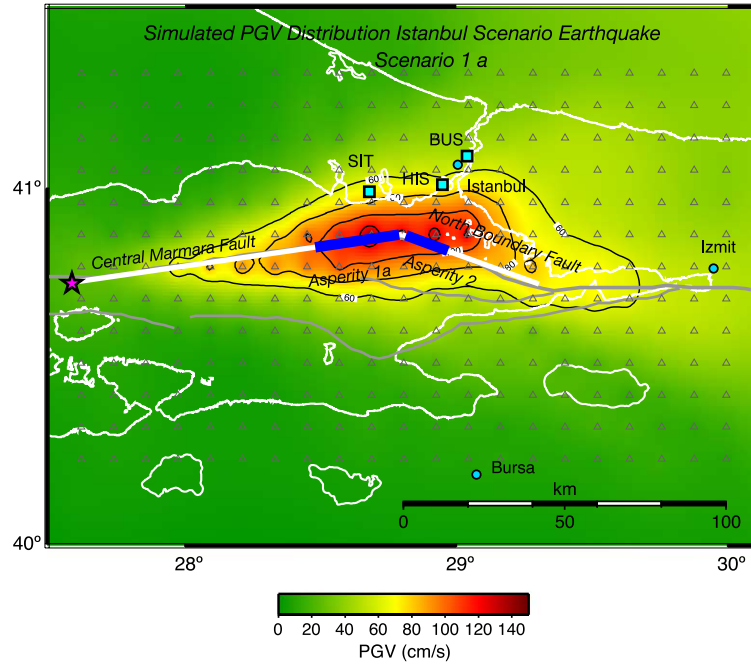


Fig. 5. Simulated bedrock PGV distribution for scenario 1a. Fault segments are shown by a white line. Asperities at each segment are shown by a blue thick line. Epicenter is show by a star.

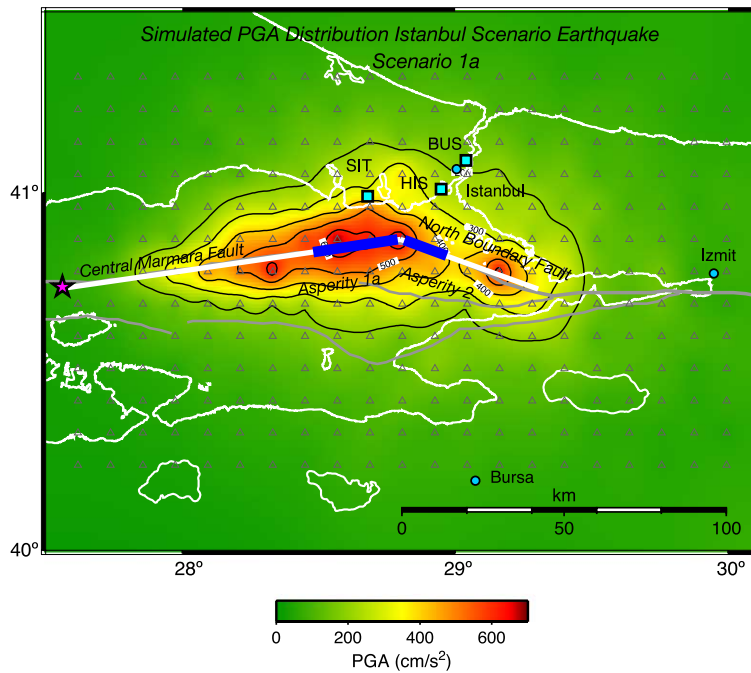


Fig. 6. Simulated bedrock PGA distribution for scenario 1a. Notation is same as in Fig. 5.

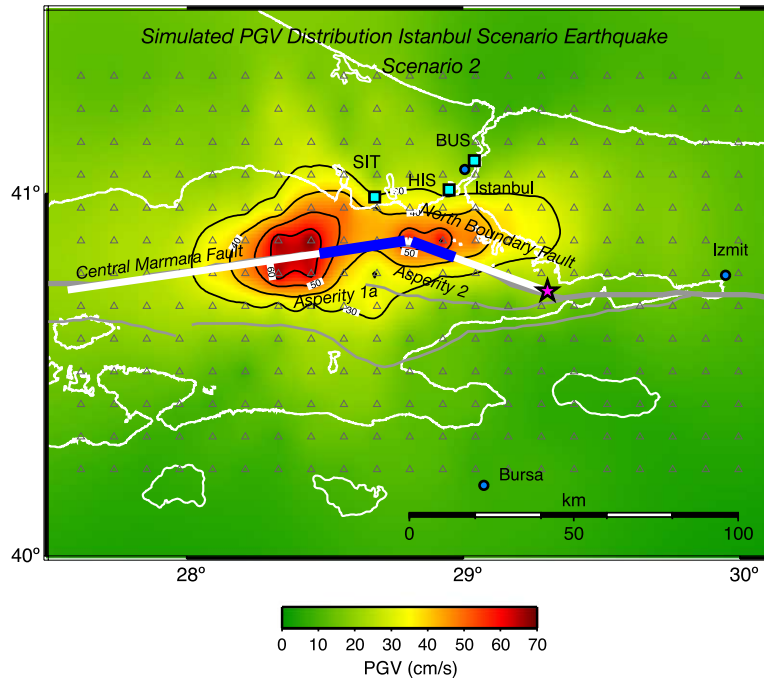


Fig. 7. Simulated bedrock PGV distribution for scenario 2. Notation is same as in Fig. 5.

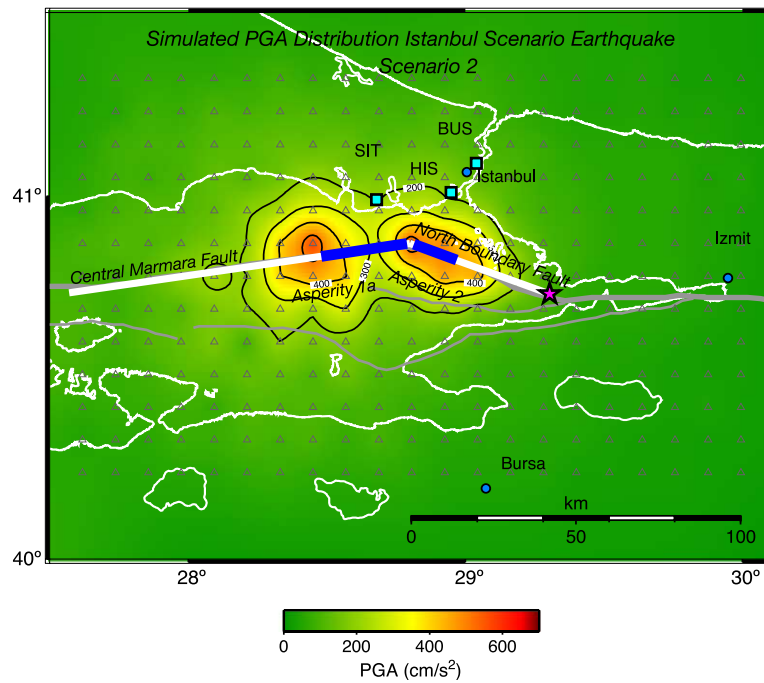


Fig. 8. Simulated bedrock PGA distribution for scenario 2. Notation is same as in Fig. 5.

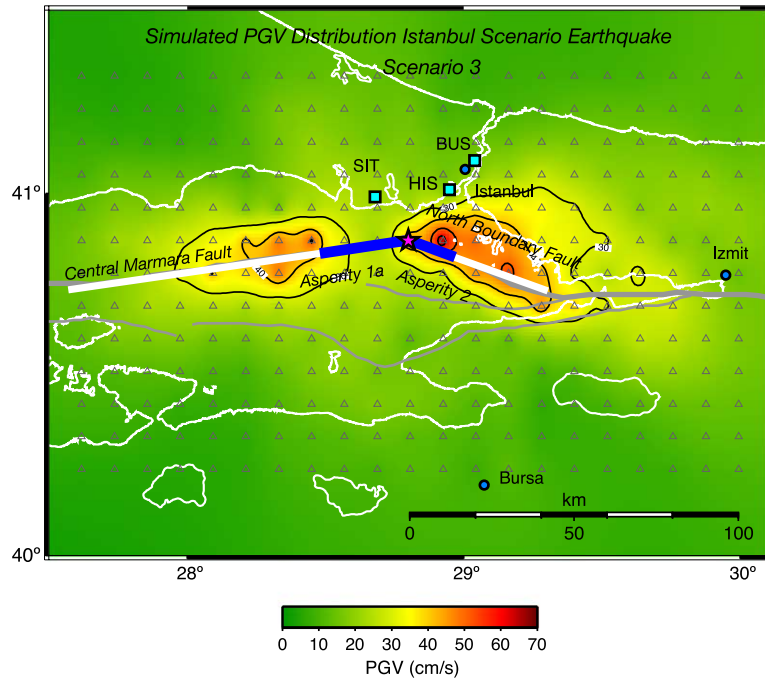


Fig. 9. Simulated bedrock PGV distribution for scenario 3. Notation is same as in Fig. 5.

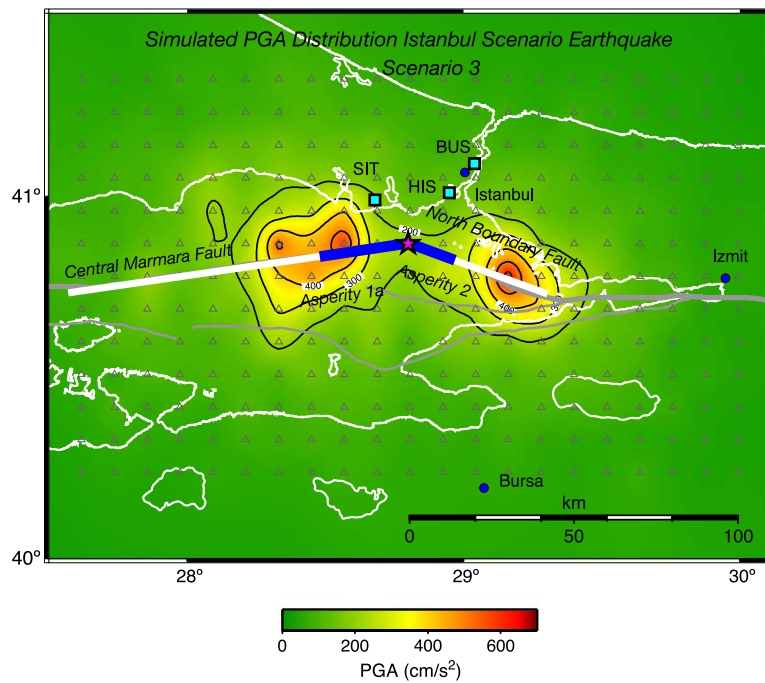


Fig. 10. Simulated bedrock PGA distribution for scenario 3. Notation is same as in Fig. 5.

frequency and thus weaker attenuation than case (1):

$$Q = 100 f^{1.5} \quad (8)$$

We calculated the ground motion at all the simulation points using the “Low Attenuation Model” for all scenario earthquakes, and selected the worst-case scenario for the Istanbul region (SIT, HIS and BUS stations). We then recalculated the ground motion for this worst-case scenario using the “Moderate Attenuation Model”.

We adopted an  $f_{max}$  value of 10 Hz, which corresponds to the upper frequency limit of our simulations. As a result, our calculations do not incorporate any strong high-frequency decay effect,

only the more moderate effects specified in Eqs. (7) or (8).

### 5. Distributions of simulated ground motion

Figs. 5–10 show the simulated PGV and PGA distribution for the scenarios 1a, 2 and 3. These distributions allowed us to identify the regions of forward source directivity for all the scenarios, which correspond to the large amplitudes. Our simulations also show that the worst-case scenario earthquake for Istanbul (scenario 1a) produces significant PGV as far away as Izmit ( $49 \text{ cm s}^{-1}$ ). This is because Izmit is located along the eastern prolongation of its fault rupture, where there would also be a large forward directivity effect.

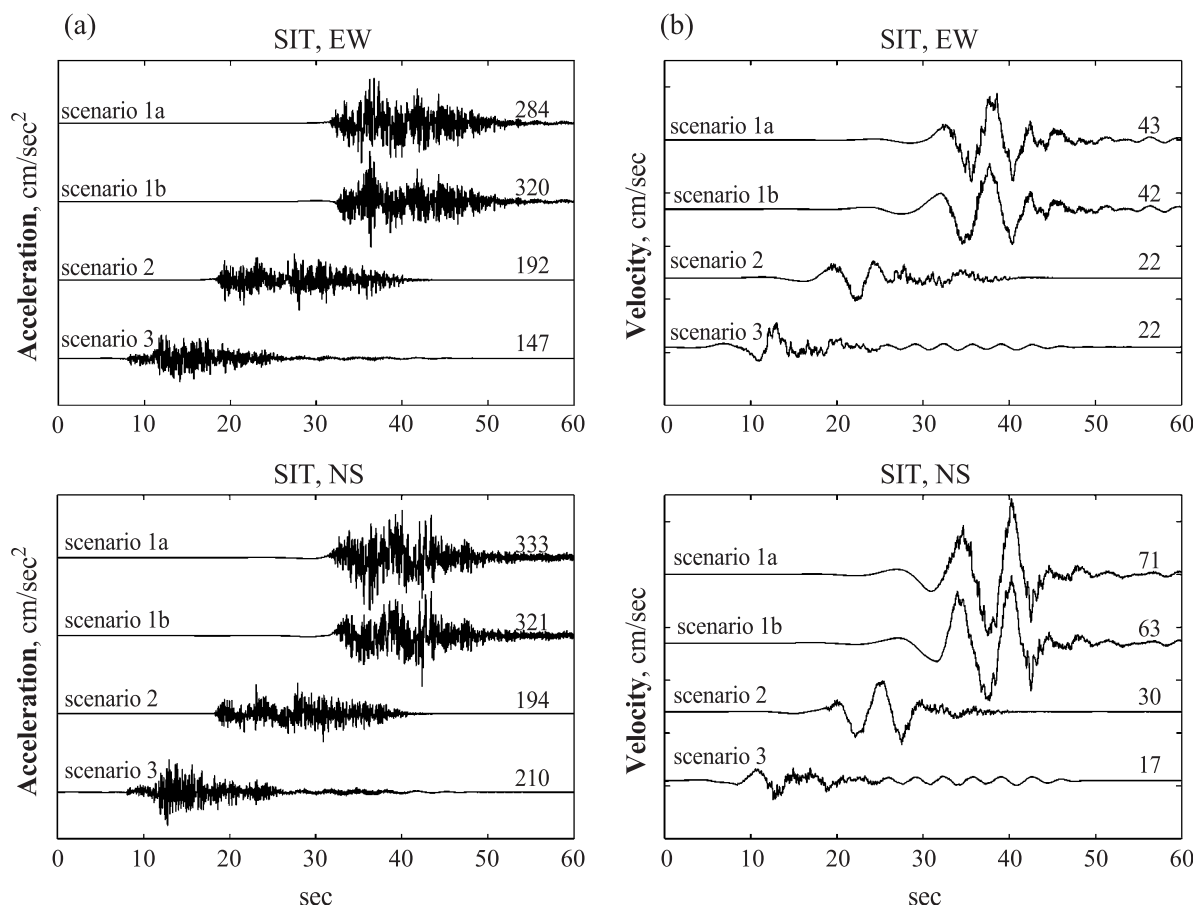


Fig. 11. EW and NS components of simulated bedrock motion at station SIT for all the scenarios for (a) acceleration and (b) velocity waveforms.

### 5.1. Ground motion at Istanbul

Comparisons of the simulated acceleration and velocity waveforms for all the scenarios, at the SIT, HIS and BUS sites in Istanbul, are shown in Figs. 11–13. Our results show that scenarios 1a and 1b produce the largest PGA ( $333 \text{ cm s}^{-2}$ ) and PGV ( $71 \text{ cm s}^{-1}$ ) in the Istanbul region. This result was expected as these scenarios involve rupture of the largest fault segment (CMF) toward Istanbul, which produces a strong source directivity effect (Figs. 5 and 6). The velocity waveforms at Istanbul, for both these scenarios, are characterized by long period forward directivity pulses of 5 to 7 s, from this forward rupture of the CMF segment. The ground motion at Istanbul is very similar from either of

these scenarios, regardless of asperity 1a being closer to Istanbul than asperity 1b. This is because Istanbul is closer to a maximum of the S-wave radiation pattern for asperity 1b than for asperity 1a. Scenario 2 produces smaller values of PGA ( $194 \text{ cm s}^{-2}$ ) and PGV ( $30 \text{ cm s}^{-1}$ ) at Istanbul (Figs. 7 and 8) because its ground motion at Istanbul is mainly controlled by the forward rupture of the NBF segment, which is shorter than the CMF segment. Scenario 3 produces the smallest values of PGA and PGV at Istanbul, as its rupture propagates away from Istanbul on both fault segments (Figs. 9 and 10). Table 3 summarizes all the PGV and PGA values at the SIT, HIS and BUS sites. Our simulated PGA values at Istanbul resemble those found from a probabilistic hazard estimation at Istanbul for a 10% probability of

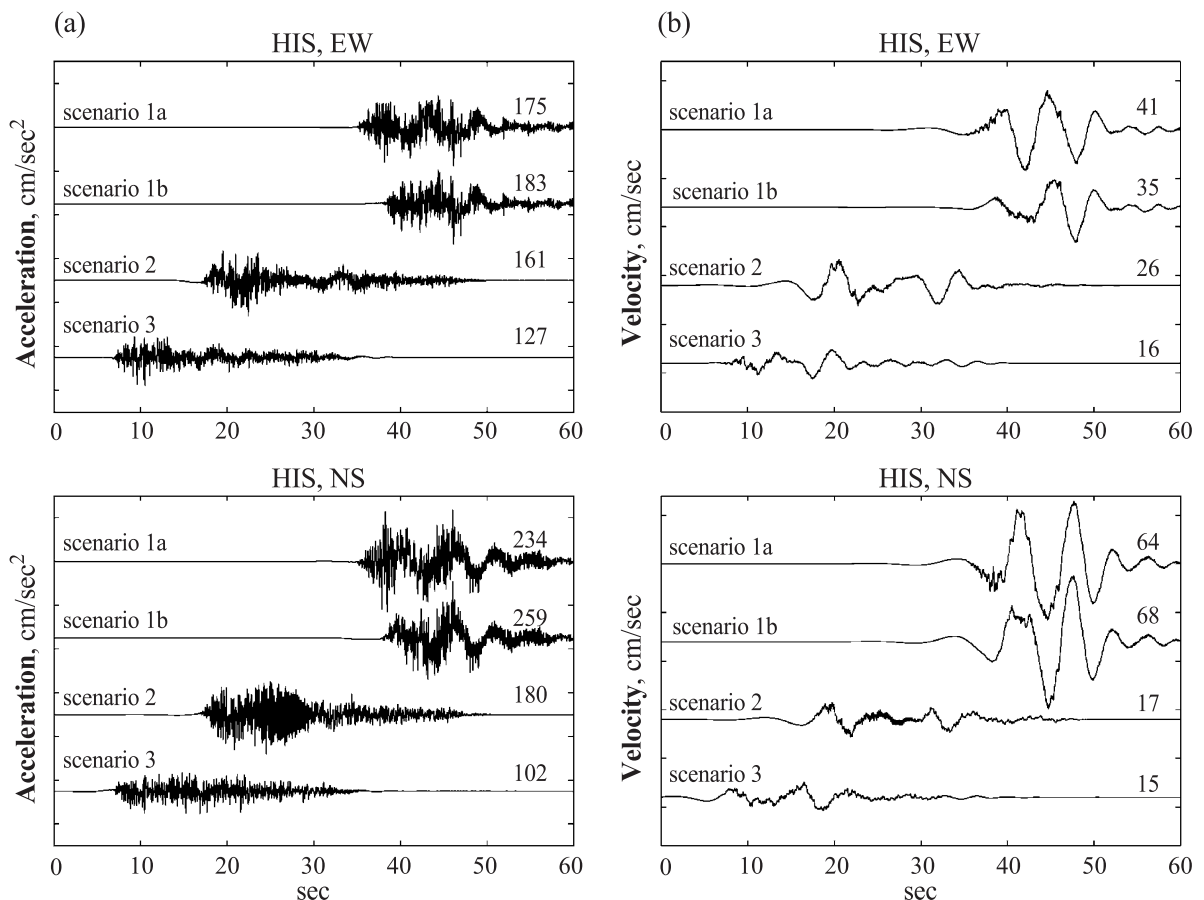


Fig. 12. EW and NS components of simulated bedrock motion at station HIS for all the scenarios for (a) acceleration and (b) velocity waveforms.

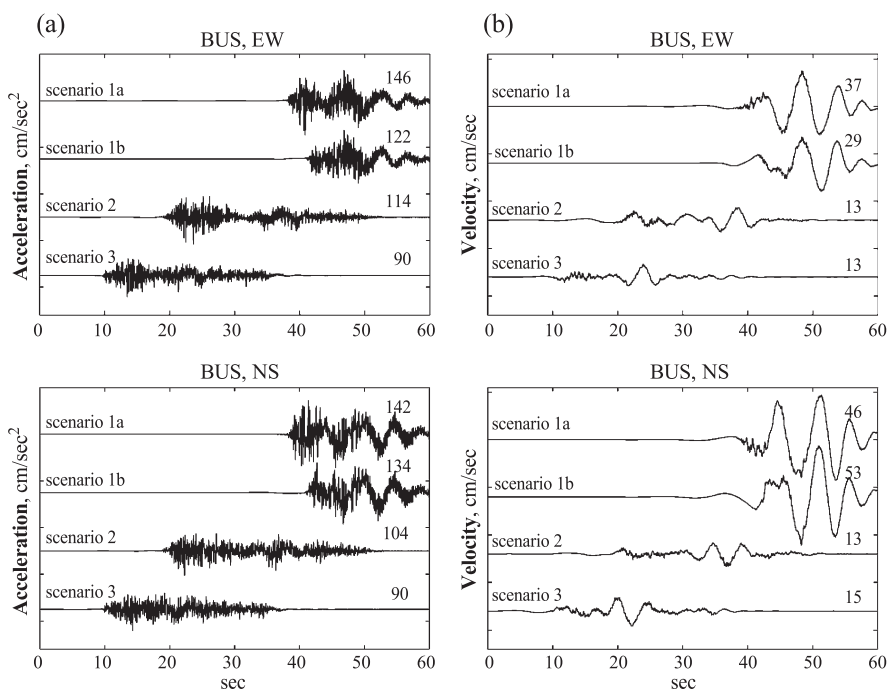


Fig. 13. EW and NS components of simulated bedrock motion at station BUS for all the scenarios for (a) acceleration and (b) velocity waveforms.

exceedence in 50 years (see Fig. 8 of Atakan et al., 2002).

Fig. 14 shows a comparison between the acceleration response spectra from all the scenario earthquakes (EW and NS components) for the SIT, HIS and BUS sites. All these spectra are characterized by large peaks at short periods (less than 1.0 s). For scenarios 1a and 1b we also observe a large long-period peak at ~4–5 s at all the sites, either in the EW or NS component (Fig. 14). This peak is also generated by the rupture of the CMF segment toward Istanbul.

### 5.2. Simulated spectra and seismic design code

Fig. 14 compares these simulated acceleration spectra with the current Turkish Seismic Design Code (TSDC) for an engineering bedrock site anchored at  $300 \text{ cm s}^{-2}$  (Aydivinoğlu, 1998). Most of the spectral values for our scenario earthquakes are within the level specified by the TSDC at short periods (<1.0 s) for the HIS and BUS stations. In the case of the SIT station, scenarios 1a and 1b produce larger spectral values than the TSDC at short periods. For periods

around 4 s, our simulations predict values significantly larger than the TSDC specification (Fig. 14). This effect, which is caused by forward directivity toward the city, may cause serious damage to high-rise buildings at Istanbul.

Furthermore, we note that our simulations are for a velocity structure in which the uppermost layer has an S-wave velocity ( $V_s$ ) of 2100 m/s (Fig. 4), which is considerably larger than in the definition of engineering bedrock in the TSDC (soil type B;  $V_s$  between 300 and 700 m/s). This suggests that a simulation that incorporates an engineering bedrock into the velocity model could predict stronger ground motion than in the present simulation. Recent studies (Ergin et al., 2004; Özel et al., 2004) have indeed calculated local site amplification effects caused by the shallow velocity structure in the Istanbul area. Such effects can result in local amplification by a factor of 10 or more at some frequencies and are the main reason why damage caused by the 1999 Izmit earthquake was more intense in some districts of this city, such as Avcýlar, than in others. Similar amplification of the seismic radiation from our scenario earthquakes

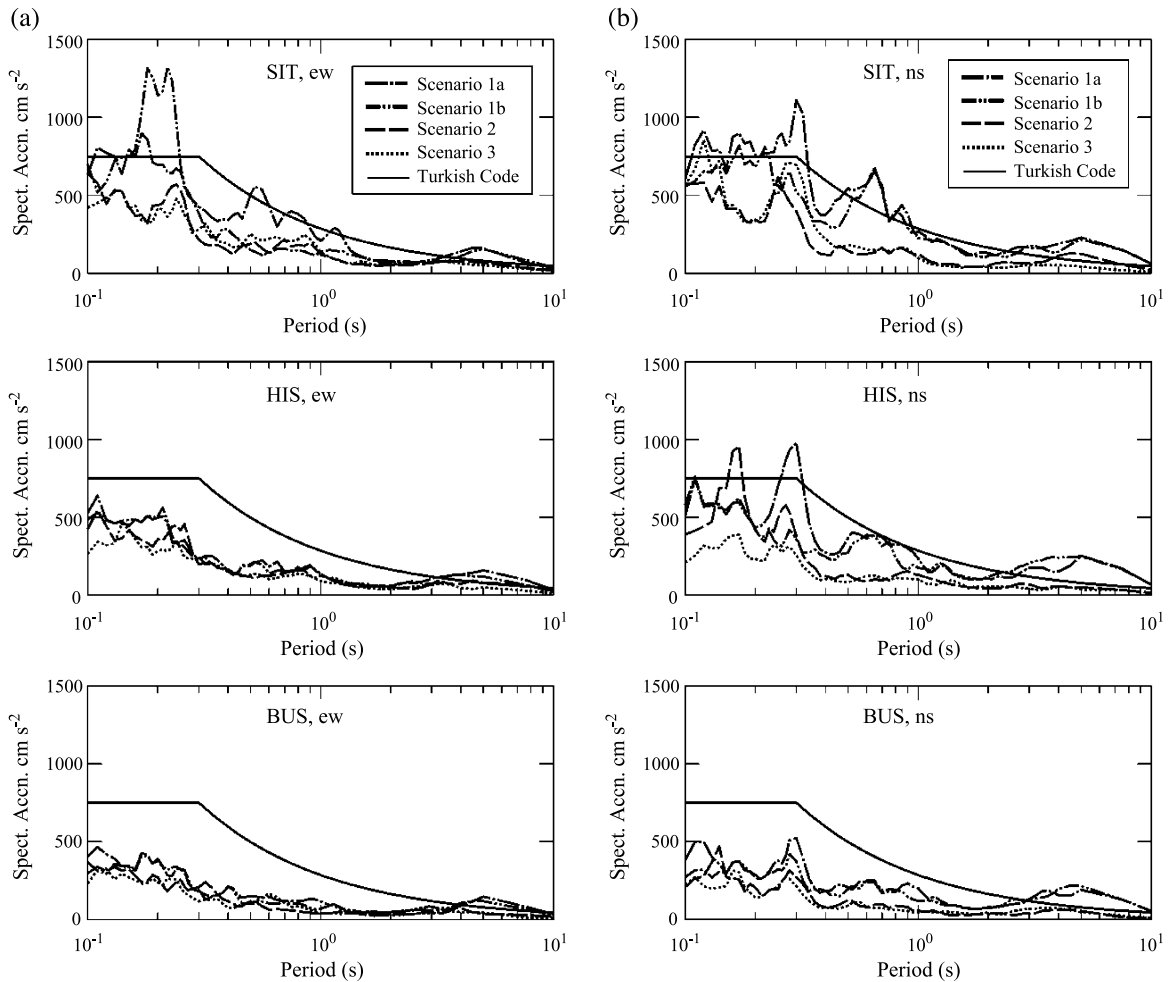


Fig. 14. Simulated bedrock acceleration response spectra at SIT, HIS and BUS for scenarios 1a, 1b, 2 and 3. (a) the EW component; (b) the NS component. The current Turkish Seismic Design Code (1998) anchored at 300 gals at zero period is shown for comparison.

would result in dramatic exceedence of the TSDC at any locality affected.

### 5.3. Attenuation of ground motion

Fig. 15 compares the attenuation with distance of our simulated PGA and PGV with three empirical attenuation relationships. For PGA, the first comparison (dashed lines) is with an empirical relationship for strike-slip earthquakes by Boore et al. (1997). This is for  $V_s$  2100 m/s, corresponding to a NEHRP class A site ( $V_s > 1500$  m/s). The second comparison (black lines) is also for strike-slip earthquakes, but assuming  $V_s > 750$  m/s (Campbell, 1997). The third

comparison (gray lines) is with a relationship derived mainly using Japanese and Californian earthquakes, for “average” site conditions (Fukushima et al., 2000).

In general, the simulated PGA values for our “Low Attenuation Model” (red dots in Fig. 15) agree reasonably well with the predictions by Campbell (1997) and Boore et al. (1997). For all the scenarios, the Campbell (1997) relationship seems to give a better fitting than the Boore et al. (1997) relationship, especially at distances  $> 30$  km. The upper box of Fig. 15(a) shows that our “Moderate Attenuation Model” (blue circles) results in systematically smaller PGA than the “Low Attenuation Model” (red dots). The empirical relationships of Campbell (1997) and Boore

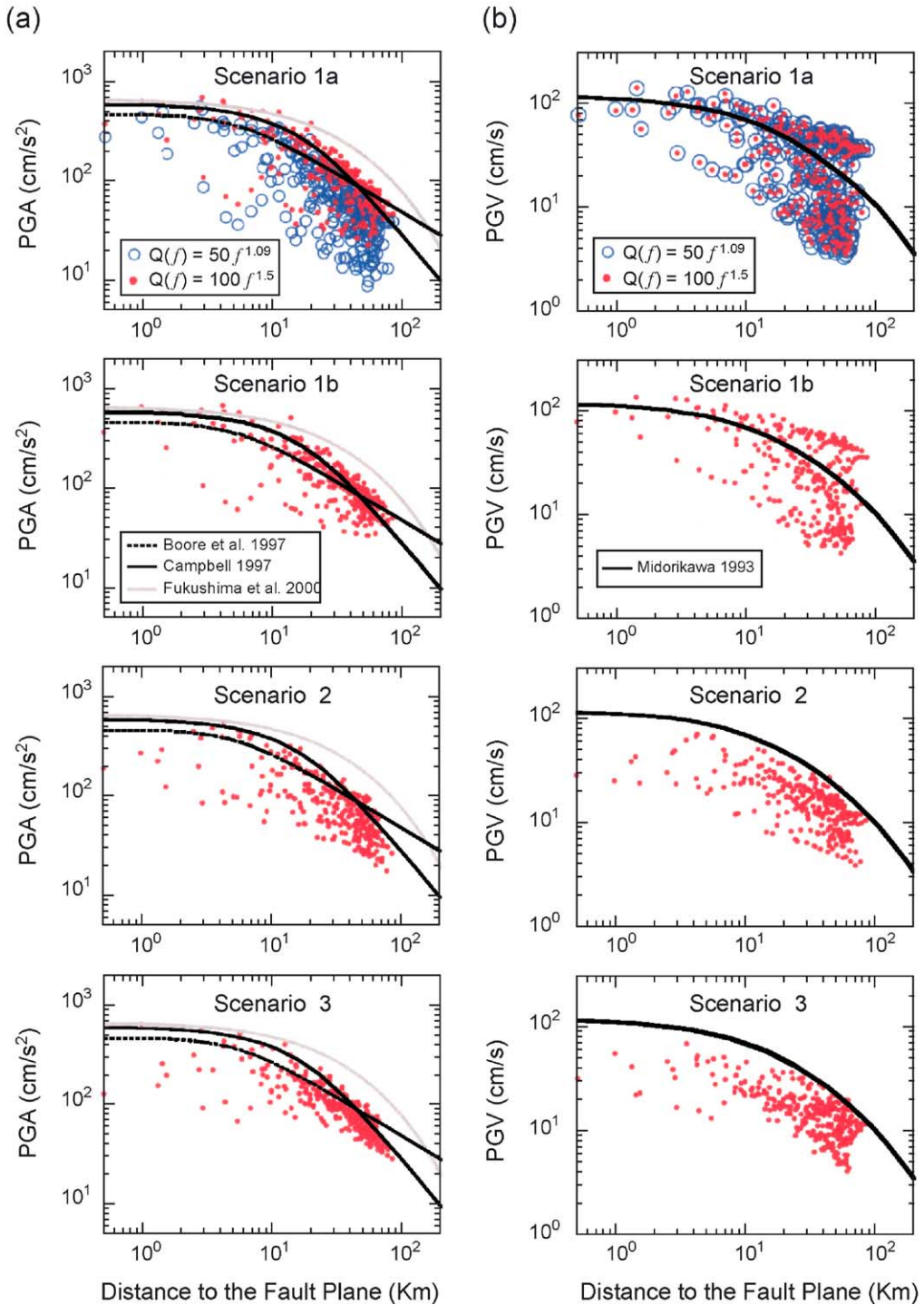


Fig. 15. (a) Comparison between the simulated bedrock PGA values with three empirical PGA attenuation relationships for all the scenario earthquakes. The red dots correspond to a “Low Attenuation Model” ( $Q=100 f^{1.5}$ ) and the small blue circles to a “Moderate Attenuation Model” ( $Q=50 f^{1.09}$ ) (b) Comparison, using the same notation, between the simulated bedrock PGV values with an empirical PGV attenuation relationship for all the scenario earthquakes.

et al. (1997) are thus in better agreement with our “Low Attenuation Model” than with this “Moderate Attenuation Model”, suggesting that this “Low Attenuation Model” is more appropriate for making empirical predictions of PGA in the Sea of Marmara region. Since our calculations assumed a velocity structure appropriate for “rock” sites, it is not surprising that our simulated PGA values are smaller than predictions using the attenuation relationship of Fukushima et al. (2000), which assumed “average” “soil” condition (Fig. 15a).

We also compared the attenuation of our simulated PGV with an empirical relationship for stiff soil conditions ( $V_s$  600m/s), by Midorikawa (1993):

$$\log \text{PGV} = -0.22M_w^2 + 3.94M_w - 13.88 \\ - \log(D + 10^{0.43M_w - 2}) - 0.002D \quad (9)$$

where  $D$  is the distance to the fault (in km) and  $M_w$  is the moment magnitude.

For scenarios 2 and 3, values from our simulation are again typically smaller than the empirical predictions. However, for scenarios 1a and 1b, the empirical prediction curve passes through the middle of the range of values from the simulations. This is because for scenarios 1a and 1b, the predictions involve sites with a strong forward directivity, whereas for scenarios 2 and 3, the directivity effect is weaker. It is also noteworthy, as indicated in the upper box of Fig. 15b, that anelasticity has a minimal effect on PGV.

#### 5.4. Variability of simulated ground motion

Figs. 11–13 indicate that the simulated ground motion has great variability between different scenario earthquakes. We evaluated this variability by calculating, at all the simulation sites, the difference between the maximum PGV and minimum PGV, divided by the minimum PGV (designated as the variability factor), for all the scenarios earthquakes, as a function of fault distance (Fig. 16). The average variability factor for the whole simulation region is nearly 2, meaning that the largest prediction of PGV is typically double the smallest prediction. This parameter represents an attempt at evaluating the uncertainty in our predictions caused by uncertainty in the source geometry and other source parameters for any possible future earthquake in the study region. It does

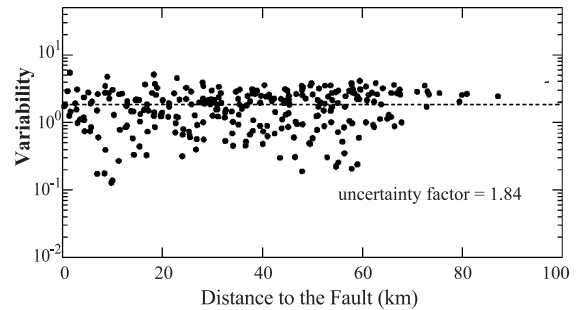


Fig. 16. Index of the variability of the simulated PGV at every simulation point in the Marmara Sea Region. This is calculated for each distance, as the difference between the maximum PGV and minimum PGV, divided by the minimum PGV. The average variability factor for the whole simulation region is nearly 2 meaning that the largest prediction of PGV is typically double the smallest prediction. This parameter represents the uncertainty in our predictions for any possible future earthquake in the study region. It does not account for the presence of site effects.

not take into account the widespread presence of unconsolidated sediments in the shallow subsurface, which as already noted, can cause dramatic amplification of strong ground motion.

## 6. Conclusions

We have undertaken a deterministic evaluation of the earthquake hazard at Istanbul. We estimated the ground motion in the Sea of Marmara region from a set of scenario earthquakes involving rupture of the entire North Anatolian Fault beneath this Sea (the CMF and NBF segments; Fig. 1). We studied the variability of the ground motion resulting from a set of fault rupture scenarios incorporating different locations of the hypocenter, different locations of the asperity within the CMF and different anelastic attenuation. Our results allow us to identify the localities likely to be affected by forward directivity of fault rupture propagation, and thus indicate that our scenarios 1a and 1b (Fig. 2) produce the largest PGA and PGV in Istanbul, as a result of rupture propagation towards this city. Our simulations probably significantly underestimate the strong ground motions that will occur in some localities because the assumed velocity structure (Fig 4) does not include any low velocity layers in the shallow subsurface. The presence of such layers will cause significant local amplification of strong ground motions. Apart from

this effect, the variability in simulated PGV for different earthquake scenarios (Fig. 16) introduces a factor of uncertainty of  $\sim 2$  in any prediction of this parameter. Anelasticity also has a significant effect on the attenuation of PGA, but not PGV, with distance. A “Low Attenuation Model” (Eq. (8)) seems to be appropriate for the Marmara region.

Our results suggest that the forward directivity of rupture propagation controls the spectral peaks in the seismic radiation, which determine acceleration response spectra, at intermediate to large periods. Our simulated response spectra (Fig. 14) are mostly within the Turkish Building Seismic Code specifications at short periods ( $< 1$  s). However, we found a large spectral peak at longer periods,  $\sim 4$  s, generated by the forward directivity of rupture propagation along the CMF segment toward Istanbul. This effect may cause damage to large buildings in this city. Furthermore, our simulations assume much higher seismic wave velocities at shallow depths than are expected across much of the Istanbul area. Such low-velocity layers will amplify strong ground motion significantly, making exceedance of the Turkish Building Seismic Code specifications likely across the period range.

## Acknowledgments

Comments from H. Yamanaka, two anonymous reviewers and the guest editors Tuncay Taymaz and Rob Westaway greatly helped to improve the manuscript. We thank Şarif Barış from the Kandilli Observatory for providing the seismic velocity model used in this study.

## Appendix A. Supplementary data

All synthetic acceleration and velocity time-series generated in this study are provided in the online data archive accompanying this journal at [doi:10.1016/j.tecto.2004.07.023](https://doi.org/10.1016/j.tecto.2004.07.023).

## References

- Akazawa, T., Kagawa, T., 2000. A study on frequency dependent radiation pattern (part 2). Fall Meeting of the Seismological Society of Japan, Abstract B12.
- Aki, K., Richards, P., 2002. *Quantitative Seismology*, 2nd ed. University Science Books, Sausalito, CA. 700 pp.
- Aksu, A., Calon, T., Hiscott, R., Yasar, D., 2000. Anatomy of the North Anatolian Fault Zone in the Marmara Sea, Western Turkey: extensional basins above a continental transform, *GSA Today*. *Geol. Soc. Amer.* 10 (6), 3–7.
- Andrews, D.J., 1989. Mechanics of fault junctions. *J. Geophys. Res.* 94, 9389–9397.
- Atakan, K., Anibal, O., Meghraoui, M., Barka, A.A., Erdik, M., Bodare, A., 2002. Seismic hazard in Istanbul following the 17 August 1999 Izmit and 12 November 1999 Duzce earthquakes. *Bull. Seismol. Soc. Am.* 92, 466–482.
- Aydinoğlu, N., 1998. Specifications for structures to be built in disaster areas: Turkish seismic design code (English Translation). Official Gazette Nos. 23098, and 23390, Ministry of Public Works and Settlement, Government of Republic of Turkey.
- Boore, D.M., 1983. Stochastic simulation of high frequency ground motions based on seismological models of the radiation spectra. *Bull. Seismol. Soc. Am.* 73, 1865–1894.
- Boore, D.M., Boatwright, J., 1984. Average body-wave radiation coefficients. *Bull. Seismol. Soc. Am.* 74, 1615–1621.
- Boore, D.M., Joyner, W., Fumal, T., 1997. Equations for estimating horizontal response spectra and peak acceleration from western North American earthquakes: a summary of recent works. *Seismol. Res. Lett.* 68, 128–153.
- Bouchon, M., 1981. A simple method to calculate Green’s functions for elastic layered media. *Bull. Seismol. Soc. Am.* 71, 959–971.
- Bouchon, M., Toksoz, M.N., Karabulut, H., Bouin, M.P., Dietrich, M., Aktar, M., Edie, M., 2002. Space and time evolution of rupture and faulting during the 1999 Izmit (Turkey) earthquake. *Bull. Seismol. Soc. Am.* 92, 256–266.
- Brune, J., 1970. Tectonic stress and the spectra of seismic shear waves from earthquakes. *J. Geophys. Res.* 75, 4997–5009.
- Campbell, K., 1997. Empirical near-source attenuation relationships for horizontal and vertical components of peak ground acceleration, peak ground velocity and pseudo-absolute acceleration response spectra. *Seismol. Res. Lett.* 68, 128–153.
- Das, S., Kostrov, B.V., 1986. Fracture of a single asperity on a finite fault: a model for weak earthquakes? In: Das, S., Boatwright, J., Scholz, C. (Eds.), *Earthquake Source Mechanism*. American Geophysical Union, Washington, pp. 91–96.
- Delouis, B., Giardini, D., Lundgren, P., Salichon, J., 2002. Joint inversion of InSar, GPS, teleseismic, and strong-motion data for the spatial and temporal distribution of earthquake slip: application to the 1999 Izmit mainshock. *Bull. Seismol. Soc. Am.* 92, 278–299.
- Dziewonski, A.M., Chou, T.A., Woodhouse, J.H., 1981. Determination of earthquake source parameters from waveform data for studies of global and regional seismicity. *J. Geophys. Res.* 86, 2825–2852.
- Ergin, M., üzalaybey, S., Aktar, M., Yalüin, M.N., 2004. Site amplification at Avcılar, Istanbul. *Tectonophysics* 391, 335–346 (this issue).
- Fukushima, Y., Irikura, K., Uetake, T., Matsumoto, H., 2000. Characteristics of observed peak amplitude for strong ground motion from the 1995 Hyogoken Nanbu (Kobe) earthquake. *Bull. Seismol. Soc. Am.* 90, 545–565.

- Fukuyama, E., Madariaga, R., 2000. Dynamic propagation and interaction of a rupture front on a planar fault. *Pure Appl. Geophys.* 157, 1959–1979.
- Gündüz, H., Ayse, K., Aysun, B., Niyazi, T., 1998. S-wave attenuation in the Marmara region, northwestern Turkey. *Geophys. Res. Lett.* 25, 2733–2736.
- Gurbuz, C., Aktar, M., Eyidogan, H., Cisternas, A., Haessler, H., Barka, A., Ergin, M., Turkelli, N., Polat, O., Ucer, S.B., Kuleli, S., Baris, S., Kaypak, B., Bekler, T., Zor, E., Bicmen, F., Yoruk, A., 2000. The seismotectonics of the Marmara region (Turkey): results from a microseismic experiment. *Tectonophysics* 316, 1–17.
- Harris, R., Dolan, J.F., Harleb, R., Day, S., 2002. A 3D dynamic stress transfer model of intraearthquake triggering. *Bull. Seismol. Soc. Am.* 92 (1), 245–255.
- Imren, C., Le Pichon, X., Rangin, C., Demirbag, E., Ecevitoglu, B., Gorur, N., 2001. The North Anatolian Fault within the Sea of Marmara: a new interpretation based on multi-channel seismic and multi-beam bathymetry data. *Earth Planet. Sci. Lett.* 186, 143–158.
- Irikura, K., 1986. Prediction of strong acceleration motion using empirical Green's function. *Proceedings of the 7th Japan. Earthq. Eng. Architectural Institute of Japan, Tokyo*, pp. 151–156.
- Kamae, K., Irikura, K., Pitarka, A., 1998. A technique for simulating strong ground motion using hybrid Green's function. *Bull. Seismol. Soc. Am.* 88, 357–367.
- Kame, N., Rice, J., Dmowska, R., 2003. Effects of prestress state and rupture velocity on dynamic fault branching. *J. Geophys. Res.* 108 (B5), 2265.
- King, G., Nabelek, J., 1985. Role of fault bends in the initiation and termination of earthquake rupture. *Science* 228, 984–987.
- Le Pichon, X., Şengör, A.M.C., Demirbağ, E., Ragin, C., Imren, C., Armijo, R., Görür, N., Catagay, N., Mercier de Lepinay, B., Meyer, B., Saatçılar, R., Tok, B., 2001. The active Main Marmara Fault. *Earth Planet. Sci. Lett.* 192, 595–616.
- Midorikawa, S., 1993. Preliminary analysis for attenuation of peak ground velocity on stiff site. *Proc. of the International Workshop on Strong Motion Data, Menlo Park, California, December 13–17, vol. 2. USGS, Menlo Park, CA*, pp. 39–48.
- Okay, A.I., Ozcan, A.K., Imren, C., Guney, A.B., Demirbağ, E., Kuscü, I., 2000. Active faults and evolving strike-slip basins in the Marmara Sea, northwest Turkey: a multichannel seismic reflection study. *Tectonophysics* 321, 189–218.
- Özel, O., Cranswick, E., Meremonte, M., Erdik, M., Safak, E., 2002. Site effects in Avcilar, west of Istanbul, Turkey from strong and weak-motion data. *Bull. Seismol. Soc. Am.* 92, 499–508.
- Özel, N.M., Sasatani, T., Oğuz Özel, O., 2004. Strong ground motion during the largest aftershock ( $M_w=5.8$ ) of the 1999 Izmit earthquake, Turkey. *Tectonophysics* 391, 347–355 (this issue).
- Pitarka, A., Kamae, K., Somerville, P., Fukushima, Y., Uetake, T., Irikura, K., 2000. Simulation of near-fault strong-ground motion using hybrid Green's function. *Bull. Seismol. Soc. Am.* 90, 566–586.
- Poliakov, A., Rice, J., Dmowska, R., 2002. Dynamic shear rupture interactions with fault bends. *J. Geophys. Res.* 107 (B11), 2295.
- Pulido, N., Kubo, T., 2004. Near-fault strong motion complexity of the 2000 Tottori earthquake (Japan) from a broadband source asperity model. *Tectonophysics* (in press).
- Sato, T., Kasahara, J., Taymaz, T., Ito, M., Kamimura, A., Hayakawa, T., Tan, O., 2004. A study of microearthquake seismicity and focal mechanisms within the Sea of Marmara (NW Turkey) using ocean bottom seismometers (OBSs). *Tectonophysics* (this issue).
- Satoh, T., 2002a. Empirical frequency-dependent radiation pattern of the 1998 Miyagiken-Nanbu earthquake in Japan. *Bull. Seismol. Soc. Am.* 92, 1032–1039.
- Satoh, T., 2002b. Radiation pattern and  $f_{max}$  of the Tottori-ken Seibu earthquake and the aftershocks inferred from KiK-Net strong motion records. *J. Struct. Constr. Eng., Archit. Inst. Jpn.* 556, 25–34. (in Japanese).
- Sekiguchi, H., Iwata, T., 2002. Rupture process of the 1999 Kocaeli, Turkey, earthquake estimated from strong-motion waveforms. *Bull. Seismol. Soc. Am.* 92, 300–311.
- Sipkin, S.A., 1982. Estimation of earthquake source parameters by the inversion of waveform data: synthetic waveforms. *Phys. Earth Planet. Inter.* 30, 242–259.
- Somerville, P., Irikura, K., Graves, R., Sawada, S., Wald, D., Abrahamson, N., Iwasaki, Y., Kagawa, T., Smith, N., Kowada, A., 1999. Characterizing crustal earthquake slip models for the prediction of strong ground motion. *Seismol. Res. Lett.* 70, 59–80.
- Straub, C., Kahle, H., Schindler, C., 1997. GPS and geologic estimates of the tectonic activity in the Marmara Sea region, NW Anatolia. *J. Geophys. Res.* 102, 27587–27601.
- Takenaka, H., Mamada, Y., Futamura, H., 2003. Near-source effect on radiation pattern of high-frequency S waves: strong SH-SV mixing observed from aftershocks of the 1997 Northwestern Kagoshima, Japan, earthquakes. *Phys. Earth Planet. Inter.* 137, 31–43.
- Wiemer, S., Wyss, M., 1997. Mapping the frequency-magnitude distribution in asperities: an improved technique to calculate recurrence times? *J. Geophys. Res.* 102, 15115–15128.
- Xu, L., Cormier, V.F., Toksoz, M.N., 2002. Complex source process of the 17 August 1999 Izmit, Turkey, earthquake. *Bull. Seismol. Soc. Am.* 92, 267–277.
- Yagi, Y., Kikuchi, M., 2000. Source rupture process of the Kocaeli, Turkey, earthquake of August 17, 1999, obtained by joint inversion of near-field data and teleseismic data. *Geophys. Res. Lett.* 27, 1969–1972.